RSC Advances

Glass structure and crystallization of Al and B containing glasses belonging to the $Li_2O–SiO_2$ system

Journal:	*RSC Advances*
Manuscript ID:	RA-ART-03-2015-004184.R1
Article Type:	Paper
Date Submitted by the Author:	01-Apr-2015
Complete List of Authors:	Gaddam, Anuraag; University of Aveiro, Department of Materials and Ceramics Engineering Fernandes, Hugo; University of Aveiro, Department of Materials and Ceramics Engineering Ferreira, José; University of Aveiro, Department of Materials and Ceramics Engineering

Glass structure and crystallization of Al and B containing glasses belonging to the $Li_2O–SiO_2$ system

Anuraag Gaddam, Hugo R. Fernandes, José M.F. Ferreira*

Department of Materials and Ceramics Engineering, University of Aveiro, CICECO, 3810-193 Aveiro, Portugal

* To whom correspondence should be addressed:

E-mail: jmf@ua.pt
Tel: 00351 234 370242
Fax: 00351 234 370204

Abstract

The aim of the present work is to investigate the effect of substituting B_2O_3 for Al_2O_3 in a non-stoichiometric lithium disilicate ($Li_2Si_2O_5$, *LS_2*) glass composition belonging to the system $Li_2O–K_2O–Al_2O_3–SiO_2$. Addition of equimolar amounts of K_2O and Al_2O_3 to binary lithium silicate glass compositions improves chemical resistance, sintering behaviour and mechanical properties of the glass-ceramics produced from sintered glass powder compacts. However, in bulk (monolithic) glasses Al_2O_3 addition hinders bulk nucleation. It also suppresses crystallization of *LS_2* and promotes formation of a meta-stable crystalline phase called lithium metasilicate (Li_2SiO_3, *LS*). The results showed that B substitution resulted in the depolymerisation of glass network increasing the percentage of NBOs leading to decreasing viscosity, molar volumes, oxygen densities and glass transition temperatures. The simultaneous mixture of Al and B into the glass composition resulted in decreased liquid-liquid phase segregation (LLPS) and lower crystal nucleation tendency when compared to Al pure or B pure compositions. Further, Al rich glasses featured lithium metasilicate crystallization at initial stages and then transformed into *LS_2* at higher temperatures, while with B addition glasses crystallize directly into *LS_2*.

1. Introduction

Glass-ceramics (*GCs*) are used in wide variety of applications ranging from military, biomedical to consumer goods like cooktops.[1] Particularly in restorative dentistry leucite and lithium disilicate (LS_2) based *GCs* are meeting the demand for excellent aesthetic and good mechanical properties with relative ease of processing.[2] These materials' compositions are carefully tailored and given controlled heat treatments to obtain desired nucleation and crystallisation of glasses. By adjusting the crystal size and fraction, required translucency and mechanical properties can be achieved. The key aspect of glass-ceramics in comparison to conventional ceramics is that they are inherently pore free which makes them well suited for high mechanical strength applications.[3] Over last four decades several fundamental studies have been performed on nucleation and crystallization of glasses belonging to various systems addressing various aspects of glass crystallization.[4–6] However, most of these studies were restricted to simple stoichiometric or binary compositions and few studies in multicomponent systems were performed only recently.[7–17] From an application point of view, in a multicomponent system, the addition of a particular dopant to the glass system changes its structure and chemistry consequently affecting its nucleation and crystallization behaviour; thereby it has a direct effect on final physical and chemical properties of *GCs*. During the initial stages of crystallization the phases that nucleate should directly depend upon local initial glass structure. Therefore, probing the bulk glass structure would offer deeper insights into the initial stages of nucleation.[18] Hence, it is imperative to understand the effect of a specific dopant on glass structure so that its crystallization behaviour can be understood in a new perspective. Therefore the current paper is mainly aimed at evaluating the effect of glass structure on crystal nucleation and overall crystallization of Al and B doped glasses.

Addition of aluminium and boron oxides to silicate glasses is known to improve chemical resistance of both glasses and *GCs*.[19] Apart from enhancing chemical resistance, Al_2O_3 also has a huge influence on the nucleation and crystallization behaviour of the glass. Several detailed studies on effect of Al_2O_3 were carried out by the authors of the present paper. [12,15,20–23] Addition of Al_2O_3 decreases phase segregation in the glass which consequentially results in the reduction of the nucleation rate.[24] Furthermore, Al_2O_3 drops the overall tendency of the glass to devitrify enhancing its glass stability and also promotes crystallization of *LS* over *LS*$_2$ When it comes to B_2O_3 addition into silicate glasses, apart from promoting chemical resistance like Al_2O_3, B_2O_3 also improves thermal shock resistance and raises electrical resistivity of the glass.[25] Contrary to the role of Al_2O_3, B_2O_3 is known to promote amorphous phase separation.[26]

Most of the commercial *GCs* used in various applications have nucleating agents added into them in order to promote higher nucleation rate and fine grained microstructure. Nonetheless, in a study like the current one, the presence of nucleating agents would make it difficult to ascertain the function of a particular dopant on the glass structure and ultimately the crystallization behaviour. Therefore, in the present study, a relatively simple multicomponent non-stoichiometric glass belonging to the system Li_2O–K_2O–Al_2O_3–SiO_2 with no nucleating agents added was chosen. In this system, the effects of substituting Al_2O_3 for B_2O_3 are elucidated. The structure of the glasses is probed employing wide range of characterization techniques. Based on the structural findings the nucleation and crystallization behaviour of these glasses were explored.

Experimental work

2.1 Preparation of glasses and glass-ceramics

Five experimental glass compositions were prepared including the base glass ($23Li_2O - 2.64K_2O - 2.64Al_2O_3 - 71.72SiO_2$) by partially replacing Al_2O_3 by B_2O_3 in steps of 25%. Accordingly, these glasses were named GB_x for x = 0, 25, 50, 75 and 100% replacement of Al_2O_3. In all the compositions molar concentrations of Li_2O, K_2O and SiO_2 were kept constant with K_2O present in the same equimolar amounts as the sum of Al_2O_3 and B_2O_3. **Table 1** presents the compositions of the experimental glasses.

For precursors, powders of technical grade SiO_2 (purity > 99%) and reagent grade Li_2CO_3 (purity > 99%), K_2CO_3 (purity > 99%), Al_2O_3 (purity > 99%) and H_3BO_3 (purity > 99%) were used. These powders were mixed homogenously by ball milling and calcined at 800 ºC in alumina crucibles for 1 h in air. The calcined powders (~100 g batch sizes) were further mixed in mortar-pestle for homogeneity and transferred to Pt-crucibles for melting at temperature of 1550 ºC for 1 h in air. Bulk (monolithic) bar shaped glasses were prepared by pouring the melt on bronze mould. To investigate LLPS, samples GB_0, GB_{50}, and GB_{100} were annealed at 520 ºC for a long duration (100 h) in order to bring the samples to thermodynamic equilibrium. Non-annealed bulk glasses were heat treated at temperatures between 650–900 ºC with 50 ºC interval at a rate of 2 K min^{-1} for 1 h in air to investigate the devitrification process.

2.2 Characterizations of the samples

Optical spectra of the bulk glasses were recorded using UV-VIS-NIR spectrophotometer (UV-3100, Shimadzu) in the range 200–800 nm wavelength with a resolution of 0.2 nm. For this, bulk glass slices of thickness 1.5−2.0 mm were cut from the bars and the both parallel sides were polished to a mirror finish. Fourier transform infrared spectroscopy (FTIR, model Mattson Galaxy S-7000) was carried out in the range of 300−1400 cm^{-1} with a resolution of 4 cm^{-1} on glass powders prepared by crushing the bulk

glass. Samples for FTIR were prepared by mixing 1/150 (by weight) portion of the sample with KBr and hand pressed to obtain pellets. Raman spectra (Bruker RFS100 FT-Raman) were recorded for the same glass powders in the range of 300−1800 cm^{-1} with a resolution of 4 cm^{-1}. The samples were excited by an infrared laser of power 350 mW with an excitation wavelength of 1064 nm. ^{29}Si and ^{27}Al magic angle spinning nuclear magnetic resonance spectroscopy (MAS-NMR, Bruker ASX 400) was conducted on selected glass samples prepared by crushing them into fine powder. ^{29}Si MAS-NMR was performed for samples GB_0, GB_{25}, GB_{50} and GB_{100} using tetramethylsilane (TMS) as a chemical shift reference. The spectrometer was operated at a Larmor frequency of 79.5 MHz with a 9.4 T magnetic field (B_o) using a 7 mm probe rotating at 5 kHz. The samples were excited with a 3.25 μs radiofrequency (*RF*) pulse equivalent to 90º flip angle using a 60 s delay time. ^{27}Al MAS-NMR was carried out on samples GB_0 and GB_{50} employing $Al(NO_3)_3$ as a chemical shift reference. The spectrometer was operated at a Larmor frequency of 104.3 MHz with a 9.4 T magnetic field (B_o) using a 4 mm probe rotating at 14 kHz. The samples were excited with a 0.7 μs *RF* pulse equivalent to 10º flip angle using a 2 s delay time. ^{11}B MAS-NMR spectra were recorded for the samples GB_{50} and GB_{100} using Hahn-echo technique with 90º and 180º pulses in order to get better resolution of the spectra. The spectrometer was operated at a Larmor frequency of 128.4 MHz with a 9.4 T magnetic field (B_o) using a 4 mm probe rotating at 14 kHz. The samples were excited with a ~6.5 μs *RF* pulse equivalent to 90º flip angle using a 1 s delay time. H_3BO_3 was used as a chemical shift reference. In order to evaluate higher coordinated Al units, ^{27}Al MAS-NMR was performed using higher magnetic field of 16.4 T (Bruker Avance III HD 700) for sample GB_{25}. For this, 4 mm probe was used rotating at 14 kHz with a 10º flip angle and delay time of 1 s. Deconvolutions of all NMR spectra were performed using Dmfit program.

Differential thermal analysis (DTA, Setaram Labsys) was carried out in air from ambient temperature to 1000 ºC with a heating rate of β = 20 K min^{-1}. For each DTA experiment, ~30 mg of non-annealed bulk glass crushed to grain sizes in the range of 500−1000 μm (collected by sieving) was used. DTA experiments were carried out using alumina crucibles with α-Al_2O_3 powder as a reference material. Dilatometry (BÄHR Thermo Analyse GmbH 2000, model DIL 801) was performed on all the bulk glass samples from room temperature to 600 ºC at 5 K min^{-1} heating rate. Prismatic samples of length ~10 mm and cross section ~3×4 mm^2 were prepared for dilatometry. Densities of all bulk glasses were measured employing Archimedes principle by immersing samples in ethylene glycol solution.

Microstructures of all glasses and *GCs* were recorded using reflected light optical microscope (Jenaphot 2000, Zeiss) and scanning electron microscope (SEM, SU-70, Hitachi). Samples for microstructural observation were polished and etched using 2 vol.% hydrofluoric acid for 60 s. Crystalline phase content in all glasses and glass-ceramic samples was determined by X-ray diffraction (XRD, Rigaku Geigerflex D/Mac, C Series) using Cu K_α radiation with 2θ varying from 10–60º steps of 0.02º s^{-1}.

3. Results

All the bulk cast glasses obtained after melting at 1550 ºC were transparent and bubble free. X-ray diffraction conducted on the glasses (not shown) revealed no crystalline phases confirming they are all amorphous. Considering the high melting temperature, at which the lighter elements (such as Li and B in the current compositions) are prone to the volatilization, weight losses of the glasses were measured before and after melting. The weight losses were

less than 0.2 %; which is a negligible value and it is within the limits of experimental errors.[25] In the case of boron, since it is present at a dopant level concentration, its volatilization would be far more negligible.[27]

3.1 MAS-NMR Spectroscopy

Figures 1a–c show the ^{29}Si, ^{27}Al and ^{11}B MAS-NMR spectra of the experimental glasses, respectively. In all three Figures, the spectra show relatively broad peaks which are tell-tale features for glasses, revealing their amorphous nature and wide distributions of bond angles and bond lengths. From ^{29}Si MAS-NMR spectra in **Fig. 1a**, it can be seen that for all glass samples, the spectra presents a peak maximum near ~ −92 ppm and a shoulder in the range of −104 to −106 ppm, corresponding to Q^3 and Q^4 units of $(SiO_4)^{-2}$ tetrahedra respectively.[28,29] By performing boron substitution, the peak corresponding to Q^4 gets more resolved by shifting to lower values of the chemical shifts i.e. from −104.4 to −106.4 ppm for 0 and 100% replacement of boron respectively. However, peak maximum corresponding to Q^3 remains unchanged in all compositions. Also all glasses show a small shoulder approximately near −80 ppm corresponding to Q^2. Between the two major peaks (i.e. −92 and −104.4 ppm), glasses GB_{25} and GB_{50} show two small shoulders; these shoulders are not present in Al pure (GB_0) or B pure (GB_{100}) compositions. Deconvolution of ^{29}Si spectra was performed in order to quantitatively determine the fractions of Si units present. For the deconvolution of ^{29}Si NMR spectra, four Gaussian line shapes were used corresponding to Q^2, Q^3, Q^4 and $Q^4(1X)$ (Q^4 connected to one X (Al or B) atom in second coordination sphere). An example of ^{29}Si deconvolution is presented in **Fig. 2a** and relative amounts of each Q unit as well as the fitting parameters are presented in **Table 2**. However, due to the complexity of current glass compositions with the formation of additional linkages such as Si−O−Al and Si−O−B leads to the creation of new Q units which strongly affect the ^{29}Si chemical shift. [29,30]

Therefore, the information obtained from the NMR deconvolution were used carefully within the limitations of experimental errors.

The ^{27}Al MAS-NMR spectra of the samples GB_0, GB_{25} and GB_{50} presented in the **Fig. 1b** show non-symmetrical peaks for GB_0 and GB_{50} and a near symmetrical peak for GB_{25} with peak maximums centred at ~52 and 56.4 ppm respectively. ^{27}Al being spin I=5/2 nuclei, experiences quadrupolar interactions with electric field gradient resulting in broadening and shifting of the peaks from the isotropic chemical shift values.[29] However, at higher magnetic fields quadrupolar effects are reduced and therefore GB_{25} shows lower quadrupolar effects and confirming the nonexistence of 5− and 6−fold coordinated Al.[31] In order to find out the true chemical shift values for GB_0 and GB_{50} the spectral deconvolution was performed using Czejeck distribution model according to Neuville *et al.*[32] by fitting one line shape. The peaks obtained have chemical shifts 58.85 and 58.84 ppm and quadrupolar coupling constants (Q_{CC}) 4.4 and 4.5 MHz for GB_0 and GB_{50} respectively. Therefore, being able to fit with one line shape and with the obtained chemical shift values, it can be concluded that majority of Al exists in 4-fold coordination. [29,31,33,34]

^{11}B MAS-NMR spectra for glasses GB_{25}, GB_{50} and GB_{100} shown in the **Fig. 1c** have one broad peak and another relatively sharper peak centred close to −1.3 ppm, each corresponding to trigonal (BO_3, B^{III}) and tetrahedral (BO_4, B^{IV}) boron species respectively.[29] The peak at −1.3 ppm can be attributed to reedmergnerite like structural units of boron where each of the tetrahedral boron is coordinated with four Si tetrahedrons. [29,35] In order to identify the relative contents of B^{III} and B^{IV} units of boron, the ^{11}B MAS-NMR spectra were deconvoluted and an example is presented in **Fig. 2b**. The line shapes were simulated by using two trigonal peaks with second-order quadrupolar effects each corresponding to symmetric (B^{IIIs}, boron with 0 or 3 bridging oxygens) and asymmetric trigonal (B^{IIIa}, boron

with 1 or 2 bridging oxygens) boron units.[36] For tetrahedral boron units a single mixed Gaussian/Lorentzian peak was used. The NMR parameters used for the deconvolution of the spectra, which are isotropic chemical shift (δ_{iso}), quadrupolar coupling constant (Q_{CC}), and quadrupolar asymmetry parameter (η) along with the relative contents of each boron species, are presented in **Table 3**.

3.2 Raman Spectroscopy

The Raman spectra of the experimental glasses are presented in **Fig. 3**. All glasses showed a broad peak between 400–600 cm^{-1} with peak maximum at ~550 cm^{-1}. Other peak positions are at wavenumbers 789, ~954 and ~1086 cm^{-1}. The assignments of these peaks are as follows: [30,37,38]

1. The broad peaks between 400−600 cm^{-1} are attributed to mixed stretching and bending modes of Si−O−Si bridging bonds.
2. The peak at 789 cm^{-1} corresponds to intertetrahedral deformation mode involving significant cation motion.
3. The peaks near ~954 cm^{-1} correspond to Si−O symmetric stretching in a structural unit with two terminal oxygens (Q^2).
4. The broad peaks ranging from 1000−1200 cm^{-1} could be attributed to both Q^3 and Q^4 units; however peak maximum at 1086 cm^{-1} indicate that Q^3 is present in bigger amounts.

3.3 FTIR

The FTIR transmittance spectra of the experimental glasses presented in **Fig. 4** also show broad peaks indicating amorphous nature of the glasses and wide distribution of Q^n units. All experimental glass compositions showed four absorption bands; of which one broad peak is

centred at ~1050 cm^{-1}. Two relatively sharper peaks appear centred at ~467 cm^{-1} and 780 cm^{-1}. These peak positions are assigned to various vibrational modes according Innocenzi: [39]

1. The low frequency band at ~470 cm^{-1} is attributed to transverse-optical (TO_1) mode ρ(Si−O−Si) correspond to rocking motions of oxygen atoms. It could also be attributed to the symmetric stretching vibrations of LiO_4 tetrahedra.
2. The band near ~780 cm^{-1} is characteristic of transverse-optical (TO_2) mode υ_s(Si−O−Si) caused by symmetric stretching of oxygen atoms.
3. The broad band at ~1050 cm^{-1} is due transverse-optical (TO_3) mode υ_{as}(Si–O–Si) appear as a result of antisymmetric stretching of the oxygen atoms. The shoulder at high frequency side of this band is also a characteristic of this mode.

3.4 UV-Visible Spectroscopy

Figure 5a shows optical transmission spectra of the experimental glasses. Apart from the strong UV absorption edge near ~300 nm in the UV region, glasses did not show any other absorption band in the examined region. The spectral curves for GB_{50}, GB_{75} and GB_{50} show almost same profile and therefore indistinguishable in the **Fig. 5a**. The band gap energy (E_g) for all the glasses was calculated using Tauc relationship given by the,

$$\alpha h\nu = A(h\nu - E_g)^n \quad (1)$$

where, $$\alpha = -\frac{1}{t} ln\, T \quad \text{(approx.)} \quad (2)$$

Here, α is the linear attenuation coefficient, T is the percent transmittance, t is the thickness of the sample, h is the Planck's constant, ν if the frequency of the photon, A is a constant related to band tailing, E_g is the band gap energy and the value of n depends on type of transition with values ½ and 2 for direct and indirect band gaps respectively. From the Tauc plots with $(\alpha h\nu)^{1/n}$ versus $h\nu$, the linear portion of each plot is extrapolated to intersect

abscissa to give optical band gaps. In the present paper indirect band baps were calculated for all experimental glasses by taking n = 2. The results of the band gaps presented in **Fig. 5b insert** and **Table 4** increase with increasing B substitution.

3.5 Physical and thermal properties of glasses

Densities of all monolithic glasses are presented in **Table 4**. The values of density (ρ), molar volume (V_m) and oxygen density (ρ_O) were calculated using following formulas:

$$V_m = \frac{M}{\rho} \tag{3}$$

and,
$$\rho_O = \frac{M_O\left(X_{Li_2O} + X_{K_2O} + 3X_{Al_2O_3} + 3X_{B_2O_3} + 2X_{SiO_2}\right)}{V_m} \tag{4}$$

Where M and ρ are molecular weight and density of the glass, M_O is the molecular weight of oxygen and X is the molar fraction of each oxide component present in each glass. Values of molar volumes and densities are presented in in **Table 4** and **Fig. 6**. Values for coefficient of thermal expansion (CTE, 200–400 ºC) and glass softening or deformation temperatures (T_d) determined from dilatometry are also presented in **Table 4** as well as the characteristic points (T_g: glass transition temperature, T_c: crystallization onset temperature, T_p: crystallization peak temperature, T_S: solidus point and T_L: liquidus point) from the DTA curves for all glasses. To identify these characteristic points, the intersection method was employed as shown in the **Fig. 7**; for T_g onset of baseline shift was used. Hrubý parameter (K_H) for glass stability [40,41] and reduced glass transition temperature [42] (T_{gr}) for the glasses were calculated by the formula:

$$K_H = \frac{T_C - T_g}{T_S - T_c} \tag{5}$$

and, $$T_{gr} = \frac{T_g}{T_L} \qquad (temp.\ in\ K) \qquad (6)$$

The percentage of non-bridging oxygens (NBOs) with respect to total number oxygens present as an indicator of polymerization of glass network for each glass composition was calculated based on the formula:

$$NBO\ (\%) = \frac{2 \times ([Li_2O] + [K_2O] - [Al_2O_3] - [B^{IV}{}_2O_3])}{[Li_2O] + [K_2O] + 3[Al_2O_3] + 3[B_2O_3] + 2[SiO_2]} \qquad (7)$$

Here all Al is assumed to be in tetrahedral coordination and the amount of B^{IV} units is obtained from ^{11}B NMR deconvolution. The values of NBO percentage are presented in **Table 4** for glass compositions GB_0, GB_{25}, GB_{50} and GB_{100}.

3.6 Microstructures and phase analysis

The non-annealed cast glasses showed small signs of liquid-liquid phase segregation (LLPS) near the edges where thermal conditions must have been prone for its occurrence. To shed further light on LLPS, the glasses were annealed at 520 ºC for 100 h. Homogenous droplet-like LLPS occurred throughout the samples in the following relative extents $GB_0 > GB_{100} > GB_{50}$, as obtained from SEM images (e.g. **Figs. 8c–d**). The size of the droplets varied from few tens to 200 nm. The LLPS was also visible macroscopically as the glasses appeared cloudy. The cloudiness was greater for Al-rich sample GB_0 compared to GB_{50} or GB_{100}. XRD analysis of annealed glass samples (not shown) revealed no crystalline phases.

The microstructures of glasses heat treated at lower temperatures (650– 700 ºC, **Fig. 9**) reveal a nucleation extent dependence on B substitution. The number of spherulitic crystals in bulk glasses (a qualitative measure of nucleation rate) displays an apparent exponential-type increase with B substitution, excepting GB_{25} that shows the lowest nucleation extent.

Extensive crystallization occurred upon heat treating the glass samples at temperatures ≥ 700 ºC as seen in the optical (**Fig. 10a–c**) and SEM (**Fig. 10d**) micrographs, with morphological features depending on B substitution and heat treatment temperature.

The X-ray diffractograms for all samples isothermally treated for 1 h at temperatures between 650–900 ºC are presented in **Fig. 11**. Transient phases are not expected under these close to thermodynamic equilibrium conditions. It can be seen that LS_2 and LS_2-*ss* (low temperature solid solution phase of LS_2) were the prominent crystalline phases formed at 650 ºC. The crystallization propensity was enhanced with increasing B substitution. Al-rich glasses tend to crystallize minor mounts of *LS* phase and retain it at higher temperatures. Increasing B substitution favoured the formation of various polymorphs of silica at higher temperature.

In order to identify any transient phases formed upon heat treating under non-isothermal conditions, the extreme compositions GB_0 and GB_{100} (particle sizes between 500−1000 μm) were subjected to a heat treatment similar to DTA (β = 20 K min^{-1}). The samples were quenched from temperatures below melting point in order to preserve any transient crystalline phase formed. The diffractograms of these samples presented in **Fig. 12b** show formation of *LS* and LS_2 in GB_0 and GB_{100} respectively. Thus the crystallization and melting peaks in DTA (**Fig. 7**) should correspond to these transient phases.

The solidus (T_S) and the liquidus (T_L) points obtained from the DTA curves plotted against the percent boron replacement and the X-ray patterns of resulting GB_0 and GB_{100} samples are displayed in **Fig. 12a-b**. With boron replacement increasing, T_L gradually decreases, while T_S remains ~constant up to GB_{25}, steeply drops for GB_{50}, being followed by a decreasing trend to constant values. Even not corresponding to equilibrium conditions, the shapes of both these curves together seem physiognomies of a phase diagram.

4. Discussions

4.1 Glass structure and properties

The structure of glasses consists essentially of Q^3 and Q^4 network forming units (**Fig. 1a**). According to earlier co-authors' studies [20,21] and other literature reports [28,30], the ^{29}Si NMR spectra of binary lithium silicate glass system ($L_{23}S_{77}$) with similar Li_2O/SiO_2 ratio (3.34) showed two very distinct peaks for Q^3 and Q^4 units with peak maximums located at approximately −92 and −108 ppm respectively. In the case of GB_0, the presence of equimolar amount of Al_2O_3 and K_2O shifts the −108 ppm peak (seen as a shoulder) to higher values. Since Al is present in this glass system in 4−fold coordination as suggested by ^{27}Al NMR results (**Fig. 1b**), the shift of −108 ppm is due to the deshielding effect on Si nuclei when Al atoms are introduced in the second coordination sphere creating $Q^4(m\text{Al})$-like units.[29,30,43] However, addition of Al had no apparent effect on Q^3 peak suggesting no possible formation of $Q^3(m\text{Al})$-like units. Hence it seems that Al forms tetrahedral units and is preferentially coordinated to Q^4 tetrahedra in the next nearest neighbourhood (NNN). According to the ^{29}Si NMR deconvolution of GB_0 (**Fig. 2a** and **Table 2**), $Q^4(1\text{X})$ unit positioned at −103.4 ppm with a shift of about 5.5 ppm from Q^4, should be assigned as $Q^4(1\text{Al})$ unit. The result of ^{29}Si NMR deconvolution for GB_0 is in accordance with deconvolution reported earlier[13] for this composition (Q^3: 74.3%, Q^4: 25.7%) where separate peaks for $Q^4(1\text{Al})$ and Q^4 were not considered but a single peak accounting to both m = 0 and 1. Because of this oversimplification, the earlier ^{29}Si NMR deconvolution results were less consistent with the chemical composition. In the present case, the relative amounts of each unit corresponding to Q^2, Q^3, $Q^4(1\text{Al})$ and Q^4 are 1, 74, 15 and 10 % respectively. According to the percentage of $Q^4(1\text{Al})$ units, the amount of Al_2O_3 in the glass composition was calculated to be ~1.32 mol%, i.e., half of total (2.64 mol%) Al_2O_3 incorporated in this glass composition. Also, the percent of Q^3 units is higher than expected for this composition. Since Al−O−Al type

linkages are prohibited according to Loewenstein's Rule in aluminosilicate networks,[44–46] the possible explanation for the underestimation of Al would be the involvement of the remaining Al atoms in the formation of other units such as $Q^4(2\text{Al})$ and $Q^4(3\text{Al})$ whose chemical shifts lie at approximately −98 and −92 ppm respectively. Therefore, the upsurge in the amount of Q^3 units is consistent with the creation of $Q^4(3\text{Al})$ units, which have same chemical shift as Q^3 units. The likelihood of the creation of $Q^4(2\text{Al})$ units was also assumed but attempts to quantify these units gave only small values. Considering the broad and overlapping peaks of Q^3 and $Q^4(1\text{Al})$, and that the inclusion of another small peak corresponding to $Q^4(2\text{Al})$ would only make deconvolution less reliable, thus this $Q^4(2\text{Al})$ peak was not taken into account. The deconvolution of GB_0 ^{29}Si NMR spectrum gave a slight (~2 mol%) underestimation of SiO_2 amount, possibly due to the occurrence of some LLPS (**Fig. 8**). The ^{29}Si nuclei present in phase segregated regions richer in SiO_2 would have spin-lattice relaxation times (T_1) extremely large in comparison to 60 s delay times used in the current NMR experiments.[47] These relaxation times can be reduced by the addition of paramagnetic impurities to glass. But our previous studies[14] showed that even small addition of paramagnetic ions had a huge influence on glass crystallization. The extent of phase separation in the current experimental glasses used for NMR was observed to be very small. **Figs. 8a-b** represent those small phase segregated regions responsible for the underestimation Si content according to ^{29}Si NMR results. To conclude, in sample GB_0, even considering a random mixing of the glass network with a diminutive phase separation, Al atoms would form tetrahedral units that are preferentially coordinated to Q^4 Si units in NNN.

Now considering the composition GB_{100} where entire Al was substituted for B, the shoulder at −104 ppm (**Fig. 1a**) shifted back to a lower value, while a small shoulder appeared near −81 ppm. According to ^{11}B NMR spectral deconvolution of GB_{100} (**Fig. 2b**, **Table 3**), ~48% B exists as B^{IV} and the rest is present as B^{III} with about a quarter of B^{III} units

in symmetric sites. The B^{IV} units can be substituted into the tetrahedral Si sites with an alkali charge compensator similarly to Al, whereas the B^{III} units can form their own network or be coordinated with Si units. Nevertheless, it is well known that in borosilicate melts borate and silicate groups undergo a random mixing with limited formation of individual networks.[48,49] The degree of this random mixing would be in the order $B^{IV} > B^{IIIa} > B^{IIIs}$. The exact information regarding the extent of this mixing can only be determined by other techniques such as ^{17}O NMR spectroscopy where bridges like Si−O−Si, Si−O−B^{IV} and Si−O−B^{III} can be obtained; however this kind of a study is out of the scope of the present paper. Nevertheless, ^{29}Si NMR spectrum is very sensitive to the B^{IV} units if they are present in NNN where Si nuclei experience similar effect of deshielding as $Q^4(m\text{Al})$ units. Nanba *et al.*[19] used the glass optical basicity concept of Duffy and Ingram[50] and hypothesized that the chemical shift of $Q^4(1X)$ would be in the order Al > B^{IV} > B^{III} > Si for each *X*. Also several studies[30,48,51] used the arguments of Brown and Shannon[52] on bond strengths and showed that B^{III} units in the NNN of Si do not show any deshielding relative to Si. Hence Si units having B^{III} units in the NNN would experience similar deshielding effect as Si NNN units; hence they cannot be easily detected by ^{29}Si NMR spectroscopy. Therefore, $Q^4(1X)$ in ^{29}Si NMR deconvolution of the sample GB_{100} (**Table 2**) corresponds to $Q^4(1\text{B})$ type unit where B here is only a B^{IV} unit. Due to greater deshielding effect of B^{IV} units compared to Al, the chemical shift of the peak $Q^4(1X)$ for the sample GB_{100} shows a slightly lower value of −104 ppm compared to GB_0. The relative amounts of Q^2, Q^3, $Q^4(1\text{B})$ and Q^4 peaks were 4, 64, 17 and 15 % respectively. 17 % of $Q^4(1\text{B})$ accounts for the total B^{IV} units obtained from ^{11}B NMR deconvolution, suggesting that, within the limits of experimental errors, no $Q^4(2\text{B})$ or $Q^4(3\text{B})$ units were formed. This means that similarly to Al, B^{IV} units are also preferentially coordinated to Q^4 units of Si in the NNN even in a randomly mixed glass network. However, a small shoulder near −81 ppm should probably correspond to $Q^3(m\text{B})$ type units with m ≥ 2 suggesting a

small fraction of B^{IV} units are coordinated to Q^3 units. Specific attempts to quantify this peak give an integrated area of less than 1% which can be neglected in a pragmatic approach. Similarly to the glass GB_0, NMR results of glass GB_{100} also gave underestimation of SiO_2 content possibly for the same reasons (i.e. the presence of LLPS). Nonetheless, the deconvolution results for both ^{11}B and ^{29}Si nuclei revealed a reasonable internal consistency with the chemical composition. The increase in FWHM of $Q^4(1X)$ peak is possibly due to the wide distribution of bond lengths and bond angles due to the presence of both B^{III} and B^{IV} units instead of a single Al in GB_0.

In glass compositions with 25−75% boron substitution, the network structure is expected to be a mixture of both endmembers GB_0 and GB_{100}. In these glasses both Al and B^{IV} units contribute to $Q^4(1X)$. Applying structural arguments discussed for the endmembers, when a given amount of Al is removed it is expected that Q^3 and $Q^4(1X)$ contents will decrease, by adding same amount B and since it preferentially create $Q^4(1B)$ units it will increase $Q^4(1X)$ content. The net result would be a gradual decrease in Q^3 and a proportional increase in the rest of the peaks. The qualitative ^{29}Si NMR deconvolution data presented in **Table 2** show a judicious agreement with this hypothesis. The factors governing the decrement in Q^3 with B substitution are the speciation extents of B into B^{III} and B^{IV} units and of Q^3 into Q^2 and Q^4 units. As quadrupolar nuclei, B requires higher magnetic fields for obtaining well resolved peaks speciation. Therefore, within the limits of these experimental errors, the ^{29}Si and ^{11}B NMR deconvolution results for glasses GB_{25} and GB_{50} were consistent with chemical composition. The FWHM of $Q^4(1X)$ peak goes through a maximum between the two endmembers due to the involvement of all three Al, B^{IV} and B^{III} units as opposed to just one or two in GB_0 and GB_{100}, respectively. The small shoulders in the region between Q^3 and Q^4 should be due to mixtures of $Q^4(1Al)$ and $Q^4(1B)$ units.

The overall effect of replacing Al by B on glass structure is that part of boron in the form of B^{IV} substitutes Al tetrahedra and most of the rest in form of B^{III} bonds to a NBO. The net effect is an increase of NBOs thus leading to a slight depolymerisation of the glass network as confirmed in **Table 4**. The percentage of NBOs shows an increasing trend from 26 to 27.5% for 0 to 100% boron replacement, respectively.

Whereas ^{29}Si NMR spectra are very sensitive to Al and B^{IV} units when present in NNN, Raman and FTIR spectra, **Fig. 3** and **Fig. 4**, do not show significant variations with Al by B substitution. This can be attributed to the minor changes in network polymerization and the considerably smaller numbers of B−O−M and Al−O−M vibrations in comparison to Si−O−Si. Nevertheless, both Raman and FTIR spectra give a consistent perception of the overall glass structure.

The small variations in band gap energy (**Fig. 5b insert, Table 4**) are noteworthy considering the small B contents. Interestingly, the band tail slopes of B-containing samples (especially for GB_{25}), are lower in comparison to that of GB_0. Optical absorption edge in glasses is generally caused by excitonic type transitions of valance electrons in NBOs to higher levels.[25,53] Therefore, an increase in the number of NBOs could lead to a decrease in energy of UV absorption. On the other hand, transitions can also occur between the extra electron of Al in a tetrahedral position and the charge compensating alkali (K) around it. Such K-Al pairing causes a significant reduction in the UV absorption edge and masks the absorption caused by NBOs. This effect should also be evident when B is present in 4–fold coordination. When B replaces Al and is present as B^{III} and B^{IV} units, as perceived from the ^{11}B NMR spectra, the sum of K-Al and K-B pairs decreases. Accordingly, the band gap energy increases even when glass network depolymerisation is enhanced.

The ionic radii of network formers in the current glass system are 0.53, 0.25, 0.15 and 0.40 Å for Al^{IV}, B^{IV}, B^{III} and Si^{IV} respectively.[54] Upon replacing Al by B, the total B goes into glass network as B^{IV} and B^{III} units having lower ionic radius than Al resulting in contraction of glass network (**Fig. 6**). The depolymerized glass network further reduces the molar volume. The variations in the molar volume and oxygen density should be strongly linked to B^{IV} to B^{III} ratio which dictates the number NBOs, B^{IV} and B^{III}. The near linear variations observed in **Fig. 6** indicate that B^{IV} to B^{III} ratio remains approximately constant in agreement ^{11}B NMR. The CTE values (**Table 4**) did not show any specific trend and exhibit a small variation with B substitution. Glass network depolymerisation causes the interstitials to be filled with modifier ions, tending to enhance the CTE. On the other hand, B−O bonds having higher bond strengths than Al−O bonds should cause a decrease in the CTE values. These two opposing effects cancel out each other, explaining the nearly constant CTE values. The structure of supercooled liquids can be approximated to the glass structure that was discussed so far. Therefore at isokom temperature of glass softening point where viscosity is ~$10^{6.6}$ Pa·s, the structure of a supercooled liquid should be similar to its glassy state. The decrease in the glass softening temperatures with B addition is an indication of decreasing viscosity, therefore clearly supporting the depolymerisation of glass network due to B substitution. However, higher B−O bond strengths do not seem to have great role on viscosity in the supercooled state.

The findings concerning the network structure of supercooled glasses will be useful for understanding the nucleation process that also occurs at deep undercooling as discussed in the following section.

4.2 Phase segregation and crystal nucleation

Nucleation of non-stoichiometric glasses is greatly influenced by the LLPS phenomena. Therefore it is of paramount interest to understand the influence of B substitution on LLPS. The role of LLPS on crystal nucleation of glasses was thoroughly investigated and clearly established by James *et al*.[24,55–58] According to their findings, compositional variations brought along the LLPS process create ideal zones for the commencement of homogenous nucleation. As shown in **Fig. 8c−d**, the size of droplets in annealed glasses ranging from 20 to 200 nm indicates that nucleation and growth occurred simultaneously at 520 ºC. These droplets should correspond to SiO_2-rich regions embedded in Li_2O-rich matrix. Borosilicate glasses are also likely to show LLPS into boron- and silicon-rich regions. But considering the small added amounts of B, the compositions should lie only within the two liquid regions of ternary alkali borosilicate phase diagram[59].

Dopants are likely to affect both kinetics and thermodynamics (Gibbs free energy, the sum of enthalpy and entropy contributions) of LLPS in glasses. [60] The main contributions to enthalpy term include: (1) heat of formation of NBOs; (2) deformation of the Si tetrahedra in the presence of alkali ions; these reactions are exothermic and endothermic respectively. Entropy is mainly related to mixing of NBO pairs and bridging oxygens (configurational entropy). LLPS is mostly enthalpy driven (endothermic deformation of the Si tetrahedral). Topping *et al*.[61] extended this concept to aluminosilicate glasses to explain the reduction of LLPS due to Al_2O_3 addition that converts NBOs into bridging oxygens with an overall charge of −1 on each AlO_4 tetrahedral unit. Being an exothermic reaction it would reduce the overall driving force for LLPS. This enthalpy-based explanation might only be part of the overall picture as it contrasts with the largest extent of LLPS observed for the present Al_2O_3-rich GB_0 glass in comparison to B-containing compositions. According to Charles[60], in a binary alkali

silicate system the entropy due to interchanges of NBO pairs and bridging oxygens of Si−O−Si type only. However, additional types of bridging oxygens (Si−O−Al, Si−O−B^{III}, Si−O−B^{IV} and B−O−B) should be created upon adding Al_2O_3 and B_2O_3. These units are likely to increase the entropy and with the mixed Al and B glasses should show the large entropy. Hence, it is hypothesised that this increase in entropy might change the free energy curve and reduce thermodynamic driving force and ultimately the extent of LLPS, explaining the observed trend $GB_0 > GB_{100} > GB_{50}$. Further work is needed in this direction with more quantitative modelling of entropy on free energy involving ^{17}O NMR in order to evaluate the influence of the various forms of bridging oxygens. Apart thermodynamic driving force, the kinetics of LLPS is also dependent on glasses' viscosity, which decreased with increasing B substitution due to the creation of additional NBOs. The thermodynamic driving force for LLPS changes in the order $GB_0 > GB_{100} > GB_{x'}$ (here x' is 25, 50 or 75) and the kinetic barrier for LLPS of glasses change in the order $GB_{100} > GB_{75} > GB_{50} > GB_{25} > GB_0$. Such B content dependence of thermodynamics and kinetics behaviours would have a direct and profound implication on the crystal nucleation rate.

The nucleation rate of crystals depends on the kinetics of LLPS where faster kinetics enhances the crystal nucleation rate by shifting the composition of the glass matrix during the process. Considering the glass samples GB_0 and GB_{100}, GB_0 has comparatively larger thermodynamic driving force but higher viscosity. Due to its lowest viscosity, GB_{100} exhibits the fastest kinetics of LLPS and the highest crystal nucleation rate in comparison to other glasses. All mixed B and Al containing glasses have lower thermodynamic driving force for LLPS in comparison to GB_0 and GB_{100}; however the kinetics barrier for LLPS decreases with increasing B substitution, and the crystal nucleation rates are expected to concomitantly increase. However, because the thermodynamic driving force goes through a minimum between the two end members GB_0 and GB_{100}, at a particular B substitution between the end

members, the crystal nucleation rate is expected to be lower than in the rest of the samples. This explains why the glass sample GB_{25} showed lowest crystal nucleation rate among all the experimental glasses (**Fig. 9**).

The crystal nucleation of the glasses is correlated to glass transition temperature by a parameter called reduced glass transition temperature T_{gr}.[42,62] Homogenous nucleation occurs in glasses for $T_{gr} < 0.58-0.60$. The increasing trend of T_{gr} values with B substitution (**Table 4**) suggests a slowdown in the nucleation rate. Crystallization of metastable LS_2-ss solid solution occurred upon heat treating glasses at 650 ºC (**Fig. 11a**). This phase commonly forms when excess mount of SiO_2 is present in comparison to LS_2 stoichiometry.[63,64] Nonetheless at higher temperatures this phase degrades and transforms from LS_2-ss into LS_2 and silica. Increased nucleation rate in non-stoichiometric phase segregated lithium silicate has been ascribed to the nucleation of LS_2-ss phase.[65] Therefore, LS_2-ss can be assumed as the nucleating phase in all glass compositions. Accordingly, a constant T_L value can be assumed for all glass compositions; considering a same nucleating phase, the T_{gr} values tend to follow T_g values which are in accordance with the nucleation rates exhibited by glasses. Therefore, the increasing T_{gr} values with B substitution can be attributed to changing crystallizing phase rather than the nucleating phase.

4.3 Morphology and phase assemblage of crystallised glasses

Al-rich glass compositions exhibited high glass stability as seen from XRD results (**Fig. 11a-b**) and with B substitution the glasses showed an increasing tendency to devitrify under isothermal conditions due to a lowering viscosity. The concomitant crystallization of *LS* and LS_2 reduces the meaningfulness of glass stability parameter K_H (**Table 4**) derived from non-isothermal (DTA) conditions explaining the apparent lack of consistency observed. The plot of T_S and T_L against B replacement (**Fig. 12a**) resembles a region of Li_2O-SiO_2 phase

diagram[66] around LS_2 stoichiometry where a transition from LS to LS_2 occurs. **Fig. 12b** shows that pure LS and LS_2 are obtained under non-isothermal conditions from the extreme compositions GB_0 and GB_{100}, respectively. Therefore, **Fig. 12a** suggests that LS and LS_2 are preferentially formed for B replacement up to 25 % and ≥ 50 %, respectively. Based on the crystallizing phases, the glasses could be divided into two groups (0−25 % and 50−100 % B substitution). In each group the K_H values follow the trend of glass stability as seen by XRD. However, a simple glass stability parameter such $T_c - T_g$ shows better accordance with XRD for all compositions. Complete LS_2 crystallization was achieved for glasses GB_0 and GB_{100} at 800 ºC and 700 ºC, respectively (**Fig. 10**). The early crystallization of LS in Al-rich end member suggests that glass becomes Si-depleted for crystallization probably due to increased liquid stability. When present, LS is a transient and transforms into LS_2 under suitable heat treatment schedule and might lead to morphological changes (**Fig. 10**).

Conclusion

The current study investigated the role of both Al and B on glass structure, phase segregation, nucleation and crystallization when added at a small concentration. The following are the broad conclusions that are drawn from the current study.

1. Al goes in to glass network in 4-fold coordination whereas B goes in as both 4- and 3-fold coordination. This B speciation resulted in the depolymerisation of glass network, increasing the percentage of NBOs.
2. Therefore, with B substitution glasses showed decreasing viscosity, molar volumes, oxygen densities and glass transition temperatures.

3. The simultaneous mixture of Al and B into the glass composition resulted in the increased configurational entropy. Therefore, in mixed Al and B glasses the increased entropy resulted in decreased driving force for LLPS.
4. Glass GB_{100} exhibited highest crystal nucleation rate compared to all the other glasses due to fastest kinetics of LLPS, while glasses containing simultaneous mixture of Al and B featured the lowest crystal nucleation rate, which is correlated with the previous conclusion.
5. In Al rich glasses lithium metasilicate crystallizes at initial stages and then transforms into LS_2 at higher temperatures. However with B addition glasses crystallize directly into LS_2.

Acknowledgment

This study was financially supported by CICECO, University of Aveiro, Portugal. Hugo R. Fernandes is grateful for the Post-Doctoral Grant (SFRH/BPD/86275/2012) from the Fundação para a Ciência e a Tecnologia (FCT), Portugal.

References

1. W. Höland and G. Beall, *Glass-ceramic Technology*, The American Ceramic Society, Westerville, Ohio, 2002.
2. S. J. Saint-Jean, in *Advanced Ceramics for Dentistry*, eds. J. Z. Shen and T. Kosmac, Butterworth-Heinemann, 225 Wyman Street, Waltham, MA 02451, USA, 2014, pp. 255–277.
3. E. D. Zanotto, *Am. Ceram. Soc. Bull.*, 2010, **89**, 19–27.
4. V. M. Fokin, E. D. Zanotto, N. S. Yuritsyn, and J. W. P. P. Schmelzer, *J. Non. Cryst. Solids*, 2006, **352**, 2681–2714.
5. E. D. Zanotto, *Int. J. Appl. Glas. Sci.*, 2013, **4**, 105–116.

6. E. D. Zanotto, *Int. J. Appl. Glas. Sci.*, 2013, **4**, 117–124.

7. S. J. Rukmani, R. K. Brow, S. T. Reis, E. Apel, V. Rheinberger, and W. Höland, *J. Am. Ceram. Soc.*, 2007, **90**, 706–711.

8. C. S. Von Clausbruch, M. Schweiger, W. Höland, V. Rheinberger, W. Holand, and V. Rheinberger, *J. Non. Cryst. Solids*, 2000, **263**, 223–229.

9. S. Krüger, J. Deubener, C. Ritzberger, and W. Höland, *Int. J. Appl. Glas. Sci.*, 2013, **4**, 9–19.

10. S. Huang, Z. Huang, W. Gao, and P. Cao, *Cryst. Growth Des.*, 2014, **14**, 5144–5151.

11. H. R. Fernandes, D. U. Tulyaganov, and J. M. F. Ferreira, *J. Mater. Sci.*, 2012, **48**, 765–773.

12. H. R. Fernandes, D. U. Tulyaganov, A. Goel, M. J. Ribeiro, M. J. Pascual, and J. M. F. Ferreira, *J. Eur. Ceram. Soc.*, 2010, **30**, 2017–2030.

13. H. R. Fernandes, D. U. Tulyaganov, A. Goel, and J. M. F. Ferreira, *J. Eur. Ceram. Soc.*, 2012, **32**, 291–298.

14. A. Gaddam, H. R. Fernandes, D. U. Tulyaganov, M. J. Pascual, and J. M. F. Ferreira, *RSC Adv.*, 2014, **4**, 13581.

15. H. R. Fernandes, D. U. Tulyaganov, I. K. Goel, and J. M. F. Ferreira, *J. Am. Ceram. Soc.*, 2008, **91**, 3698–3703.

16. S. Huang, Z. Huang, W. Gao, and P. Cao, *Sci. Rep.*, 2015, **5**, 9159.

17. S. Huang, B. Zhang, Z. Huang, W. Gao, and P. Cao, *J. Mater. Sci.*, 2012, **48**, 251–257.

18. E. Müller, K. Heide, and E. D. Zanotto, *Zeitschrift für Krist.*, 1992, **200**, 287–294.

19. T. Nanba, M. Nishimura, and Y. Miura, *Geochim. Cosmochim. Acta*, 2004, **68**, 5103–5111.

20. H. R. Fernandes, D. U. Tulyaganov, A. Goel, and J. M. F. Ferreira, *J. Therm. Anal. Calorim.*, 2011, **103**, 827–834.

21. H. R. Fernandes, University of Aveiro, 2012.

22. H. R. Fernandes, D. U. Tulyaganov, and J. M. F. Ferreira, *J. Therm. Anal. Calorim.*, 2013, **112**, 1359–1368.

23. H. R. Fernandes, D. U. Tulyaganov, M. J. Pascual, and J. M. F. Ferreira, *Ceram. Int.*, 2014, **40**, 129–140.

24. E. D. Zanotto and A. F. Craievich, *J. Mater. Sci.*, 1981, **16**, 973–982.

25. J. Shelby, *Introduction to glass science and technology*, The Royal Society of Chemistry, Thomas Graham House, Science Park, Milton Road, Cambridge CB4 OWF, UK, 2nd edn., 2005.

26. W. Vogel, *Structure and Crystallization of Glasses*, Pergamon Press, Vieweg & Sohn GmbH, Burgplatz 1, Braunschweig, Leipzig., 1971.

27. J. A. C. van Limpt, Eindhoven University of Technology, 2007.

28. C. M. Schramm, B. H. W. S. De Jong, and V. E. Parziale, *J. Am. Chem. Soc.*, 1984, **106**, 4396–4402.

29. K. J. D. MacKenzie and M. E. Smith, *Multinuclear solid-state NMR of inorganic materials*, Pergamon, Amsterdam, 1st edn., 2002.

30. Bunker B.C., D. R. Tallant, R. J. Kirkpatrick, and G. l. Turner, *Phys. Chem. Glas.*, 1990, **31**, 30–41.

31. J. F. Stebbins, S. Kroeker, S. K. Lee, and T. J. Kiczenski, *J. Non. Cryst. Solids*, 2000, **275**, 1–6.

32. D. R. Neuville, L. Cormier, and D. Massiot, *Geochim. Cosmochim. Acta*, 2004, **68**, 5071–5079.

33. H. A. Abo-Mosallam, R. G. Hill, N. Karpukhina, and R. V Law, *J. Mater. Chem.*, 2010, **20**, 790–797.

34. R. J. Kirkpatrick, R. Oestrike, C. A. J. Weiss, K. A. Smith, and E. Oldfield, *Am. Mineral.*, 1986, **71**, 705–711.

35. B. G. Parkinson, D. Holland, M. E. Smith, a P. Howes, and C. R. Scales, *J. Phys. Condens. Matter*, 2007, **19**, 415114.

36. J. F. Emerson and P. J. Bray, in *Experimental Techniques of Glass Science*, eds. C. J. Simmons and O. H. El-Bayoumi, The American Ceramic Society, Westerville, Ohio, 1st edn., 1993, pp. 77–99.

37. D. Manara, A. Grandjean, and D. R. Neuville, *Am. Mineral.*, 2009, **94**, 777–784.

38. D. W. Matson, S. K. Sharma, and J. A. Philpotts, *Am. Mineral.*, 1986, **71**, 694–704.

39. P. Innocenzi, *J. Non. Cryst. Solids*, 2003, **316**, 309–319.

40. A. Hrubý, *Czechoslov. J. Phys.*, 1972, **22**, 1187–1193.

41. A. Cabral Jr, C. Fredericci, and E. Zanotto, *J. Non. Cryst. Solids*, 1997, **219**, 182–186.

42. V. V. M. Fokin, E. D. Zanotto, and J. W. P. J. Schmelzer, *J. Non. Cryst. Solids*, 2003, **321**, 52–65.

43. E. Lippmaa, M. Magi, A. Samoson, M. Tarmak, and G. Engelbardtlb, *J. Am. Chem. Soc.*, 1981, **103**, 4992–4996.

44. W. Loewenstein, *Am. J. Sci.*, 1954, **39**, 92–96.

45. J. A. Tossell, *Am. Mineral.*, 1993, **78**, 911–920.

46. A. V. Larin, *Phys. Chem. Miner.*, 2013, **40**, 771–780.

47. L. Martel, D. Massiot, and M. Deschamps, *J. Non. Cryst. Solids*, 2014, **390**, 37–44.

48. R. Martens and W. Müller-Warmuth, *J. Non. Cryst. Solids*, 2000, **265**, 167–175.

49. L. Du and J. F. Stebbins, *J. Phys. Chem. B*, 2003, **3**, 10063–10076.

50. J. A. Duffy and M. D. Ingram, *J. Non. Cryst. Solids*, 1976, **21**, 373–410.

51. K. L. Geisinger, R. Oestrike, A. Navrotsky, G. L. Turner, and R. J. Kirkpatrick, *Geochim. Cosmochim. Acta*, 1988, **52**, 2405–2414.

52. I. D. Brown and R. D. Shannon, *Acta Crystallogr. Sect. A*, 1973, **29**, 266–282.

53. J. Wong and C. A. Angell, *Glass Structure by Spectroscopy*, Marcel Dekker, 270 Madison Avenue, New York, 1976.

54. R. Shannon, *Acta Crystallogr. Sect. A*, 1976, **32**, 751–767.

55. E. D. Zanotto, A. F. Craievich, and P. F. James, *J. Phys.*, 1982, **43**, 107–110.

56. A. F. Craievich, E. D. Zanotto, and P. F. James, *Bull. Soc. Fr. Min. Cris.*, 1983, **106**, 169–184.

57. E. D. Zanotto, P. F. James, and A. F. Craievich, *J. Mater. Sci.*, 1986, **21**, 3050–3064.

58. A. Ramsden and P. James, *J. Mater. Sci.*, 1984, **19**, 1406–1419.

59. W. Haller, D. H. Blackburn, F. E. Wagstaff, and R. J. Charles, *J. Am. Ceram. Soc.*, 1970, **53**, 34–39.

60. R. J. Charles, *Phys. Chem. Glas.*, 1969, **10**, 169–178.

61. J. Topping and M. Murthy, *J. Am. Ceram. Soc.*, 1973, **56**, 270–275.

62. E. D. Zanotto, *J. Non. Cryst. Solids*, 1987, **89**, 361–370.

63. F. P. Glasser, *Phys. Chem. Glas.*, 1967, **8**, 224–232.

64. A. R. West and F. P. Glasser, in *Advances in nucleation and crystallization in glasses*, eds. L. L. Hench and S. W. Freiman, The American Ceramic Society, Columbus, Ohio, United States, 5th edn., 1971, pp. 151–165.

65. E. D. Zanotto and P. James, *Glas. Ber*, 1983, **56k**, 794–799.

66. F. C. Kracek, *J. Phys. Chem.*, 1930, **34**, 2641–2650.

Figure Captions

Fig. 1 Multinuclear NMR spectra of (a) ^{29}Si, (b) ^{27}Al and (c) ^{11}B of bulk non-annealed experimental glasses. (▬: B_o = 9.4 T and ▬ ▬ ▬: B_o = 16.4 T)

Fig. 2 Deconvolution of (a) ^{29}Si nuclei of GB_0 and (b) ^{11}B nuclei of GB_{100} NMR spectra.

Fig. 3 Raman spectra of experimental glasses.

Fig. 4 FTIR spectra of experimental glasses.

Fig. 5 (a) UV-Visible spectra and (b) optical band gaps of experimental glasses.

Fig. 6 Molar volumes (V_m, ◇) and oxygen densities (ρ_O, ■) of experimental glasses as a function of boron replacement.

Fig. 7 DTA curve of glass ***GB*$_{75}$** at heating rate of 20 ºC min^{-1}.

Fig. 8 Metastable liquid-liquid phase segregation of (a) & (b) non-annealed glasses and (c) & (d) annealed at 520 ºC for 100 hours.

Fig. 9 Optical microscope images showing degree of nucleation with B substitution.

Fig. 10 Micrographs of: (a) – (c) optical microscopy of completely crystallized glasses; (d) SEM morphology of spherulite crystals.

Fig. 11 X-ray diffraction patterns of crystallized glasses at temperatures: (a) 650 ºC, (b) 700 ºC, (c) 800 ºC and (d) 900 ºC (●: Lithium disilicate ($Li_2Si_2O_5$, ICDD 04-009-4359); ○: Lithium metasilicate (Li_2SiO_3, ICDD 00-029-0828); ✧: Cristobalite (SiO_2, ICDD 01-082-0512); ▽: Tridymite (SiO_2, ICDD 01-074-8988); ⮟: Quartz (SiO_2, ICDD 01-082-0512); ★: Lithium disilicate solid solution ($Li_2Si_{2+x}O_{5+2x}$, West *et al.*[64] and Glasser[63]).

Fig. 12 (a) Variation of solidus and liquidus points as a function of boron replacement. (b) Corresponding XRD patterns for glasses ***GB*$_0$** and ***GB*$_{100}$** below solidus curve. ●: lithium disilicate ($Li_2Si_2O_5$, ICDD 01-070-4056); ○: lithium metasilicate (Li_2SiO_3, ICDD 01-049-0803); ✧: cristobalite (SiO_2, ICDD 01-089-3607).

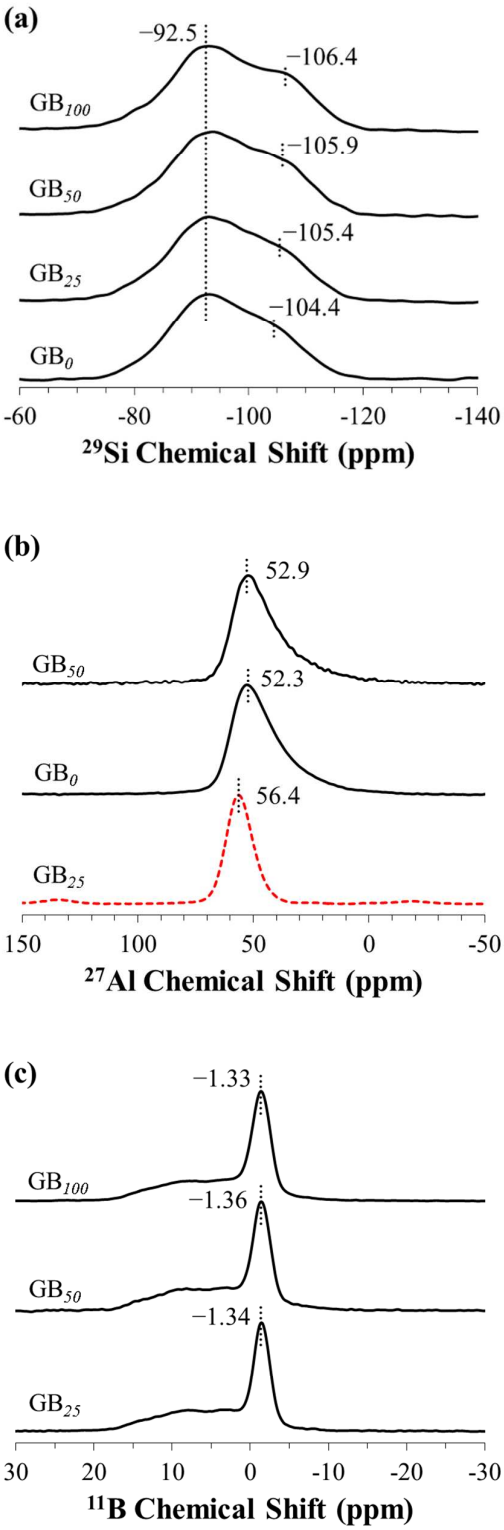
(a)
−92.5
−106.4
GB100
−105.9
GB50
−105.4
GB25
−104.4
GB0
-60
-80
-100
-120
-140
29Si Chemical Shift (ppm)
(b)
52.9
GB50
52.3
GB0
56.4
GB25
150
100
50
0
-50
27Al Chemical Shift (ppm)
(c)
−1.33
GB100
−1.36
GB50
−1.34
GB25
30
20
10
0
-10
-20
-30
11B Chemical Shift (ppm)

Fig. 1

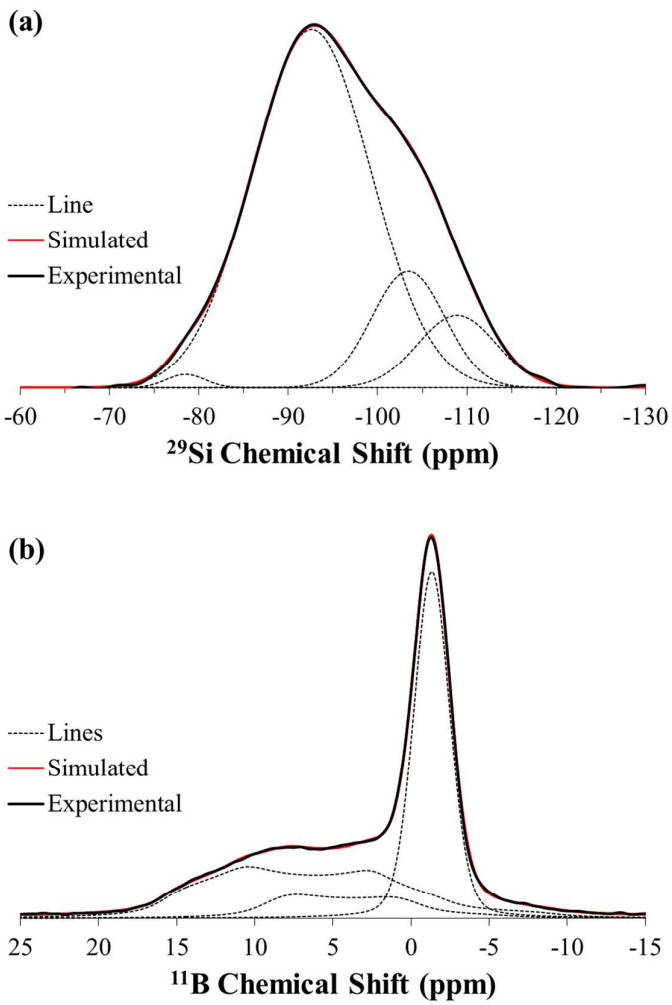
(a)
Line
Simulated
Experimental
-60
-70
-80
-90
-100
-110
-120
-130
29Si Chemical Shift (ppm)
(b)
Lines
Simulated
Experimental
25
20
15
10
5
0
-5
-10
-15
11B Chemical Shift (ppm)

Fig. 2

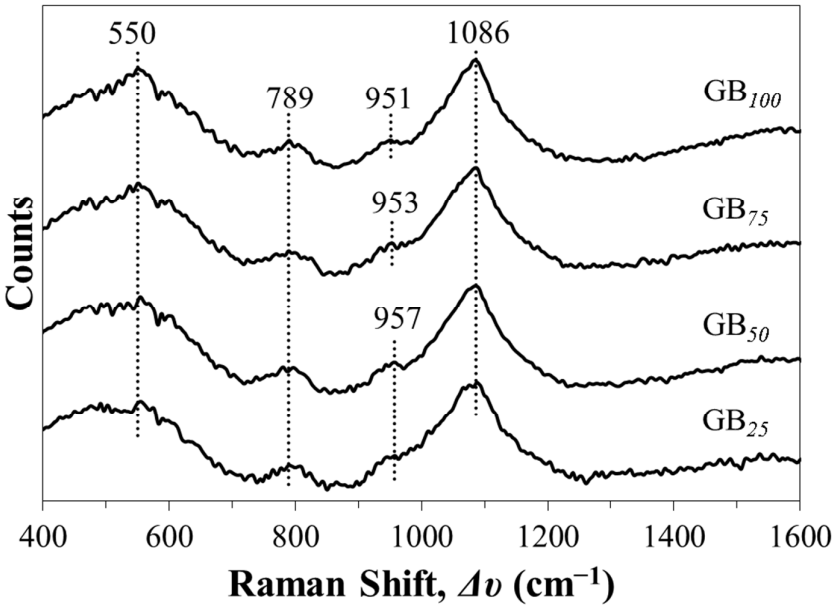
550
1086
789
951
953
957
GB100
GB75
GB50
GB25
Counts
400
600
800
1000
1200
1400
1600
Raman Shift, Δv (cm−1)

Fig. 3

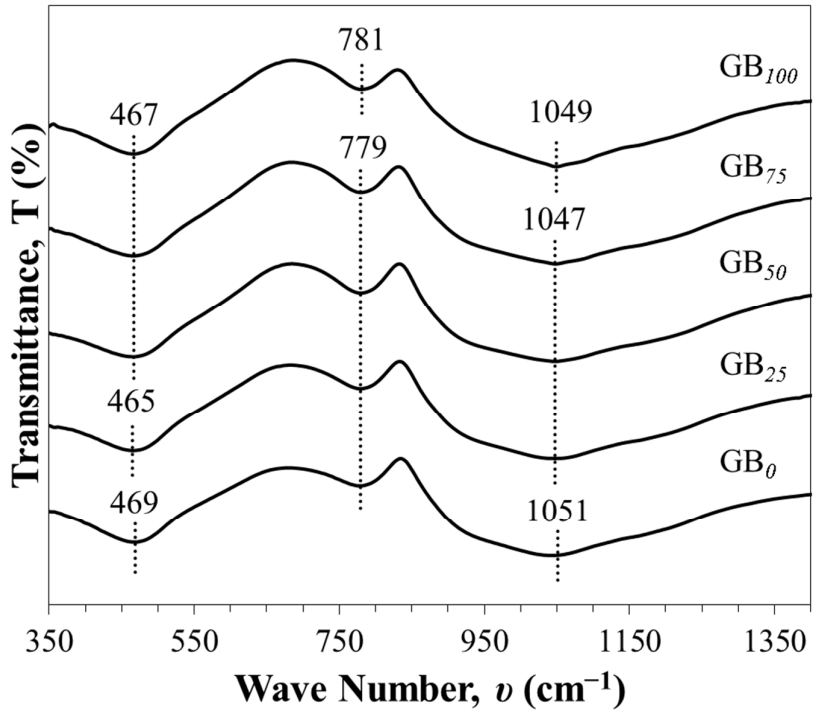
781
467
1049
779
1047
465
469
1051
GB100
GB75
GB50
GB25
GB0
Transmittance, T (%)
350
550
750
950
1150
1350
Wave Number, υ (cm−1)

Fig. 4

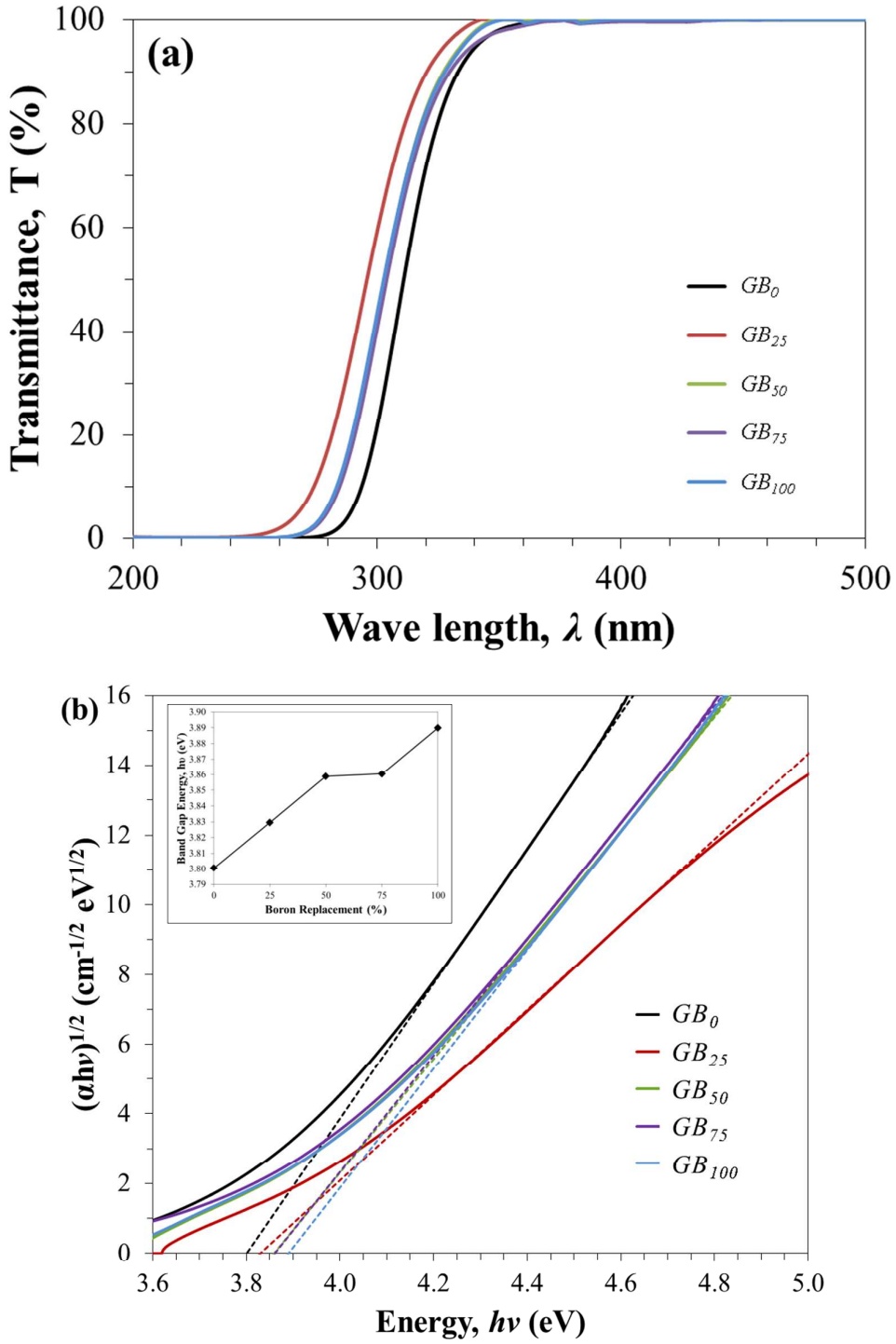
(a)
Transmittance, T (%)
Wave length, λ (nm)
GB0
GB25
GB50
GB75
GB100
(b)
(αhν)1/2 (cm-1/2 eV1/2)
Energy, hν (eV)
Band Gap Energy, hυ (eV)
Boron Replacement (%)

Fig. 5

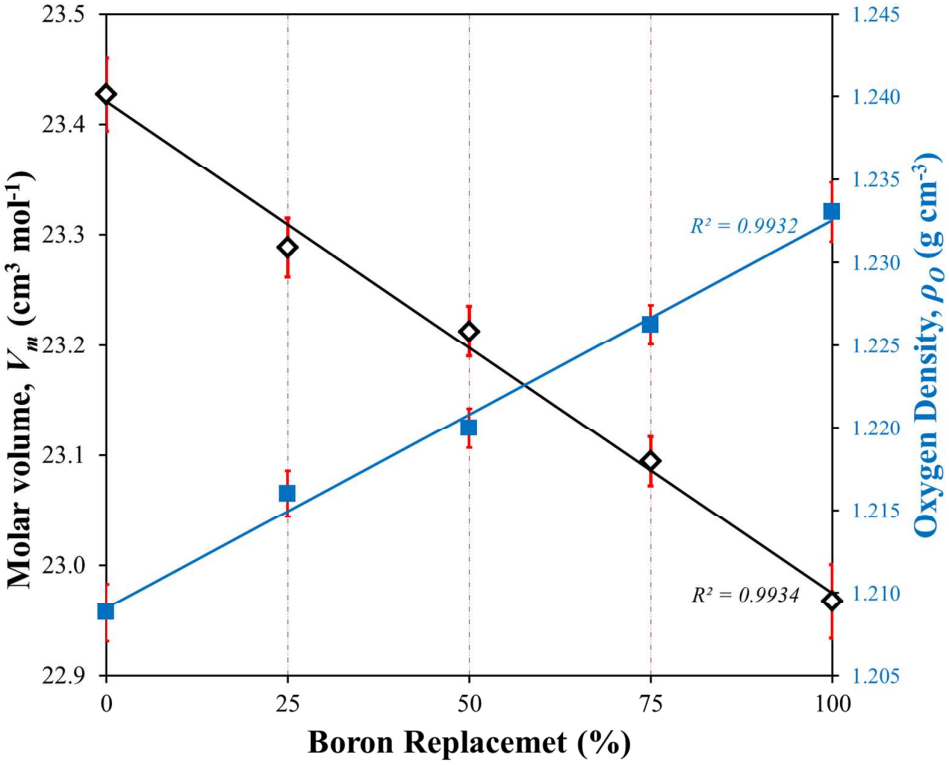
23.5
23.4
23.3
23.2
23.1
23.0
22.9
1.245
1.240
1.235
1.230
1.225
1.220
1.215
1.210
1.205
0
25
50
75
100
Molar volume, V_m (cm^3 mol^{-1})
Oxygen Density, ρ_O (g cm^{-3})
Boron Replacemet (%)
R^2 = 0.9932
R^2 = 0.9934

Fig. 6

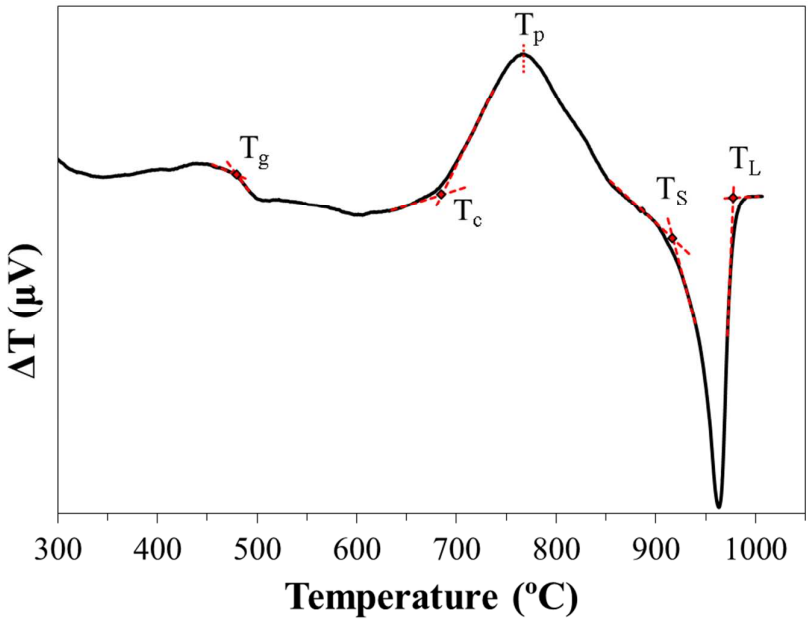
T_p
T_g
T_c
T_S
T_L
ΔT (μV)
300
400
500
600
700
800
900
1000
Temperature (°C)

Fig. 7

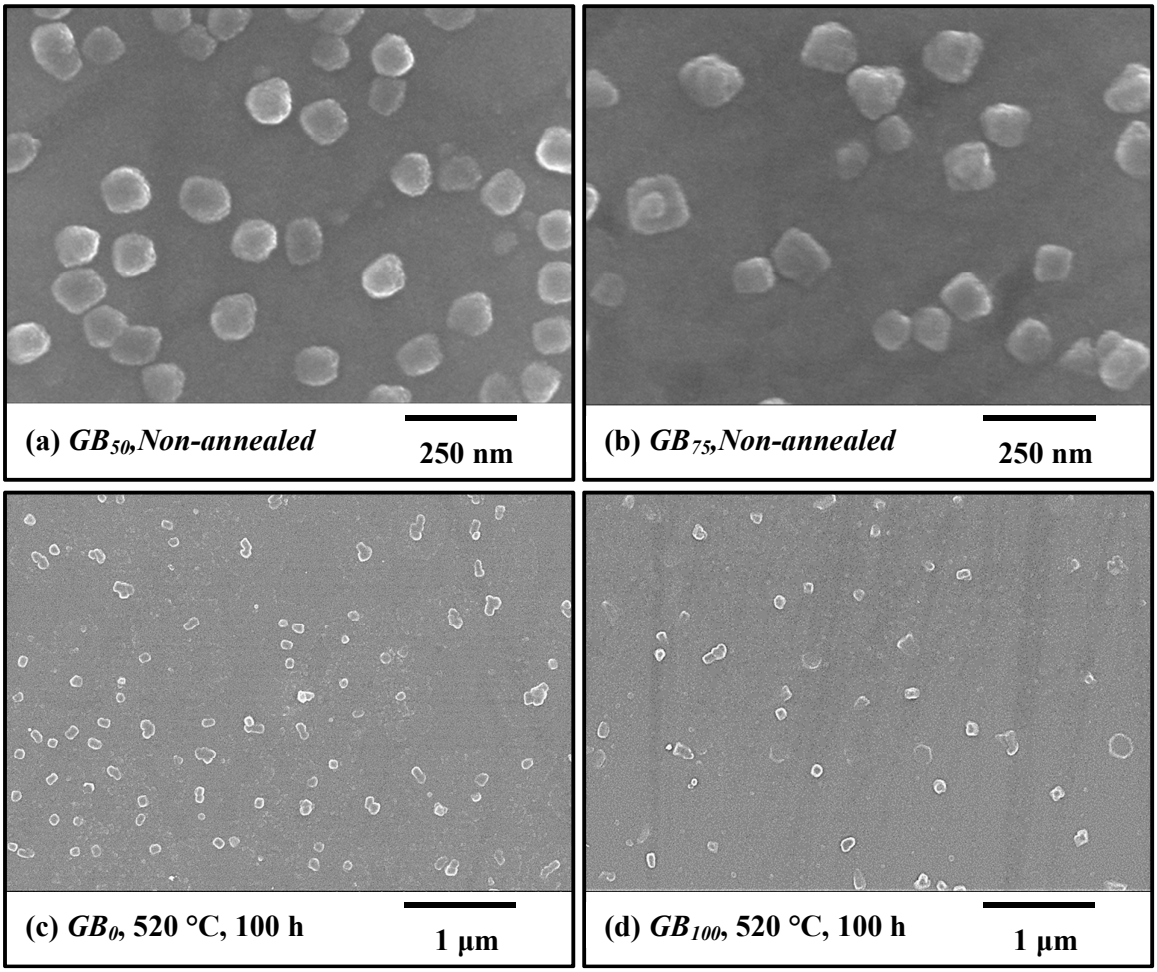
(a) GB50,Non-annealed
250 nm
(b) GB75,Non-annealed
250 nm
(c) GB0, 520 °C, 100 h
1 µm
(d) GB100, 520 °C, 100 h
1 µm

Fig. 8

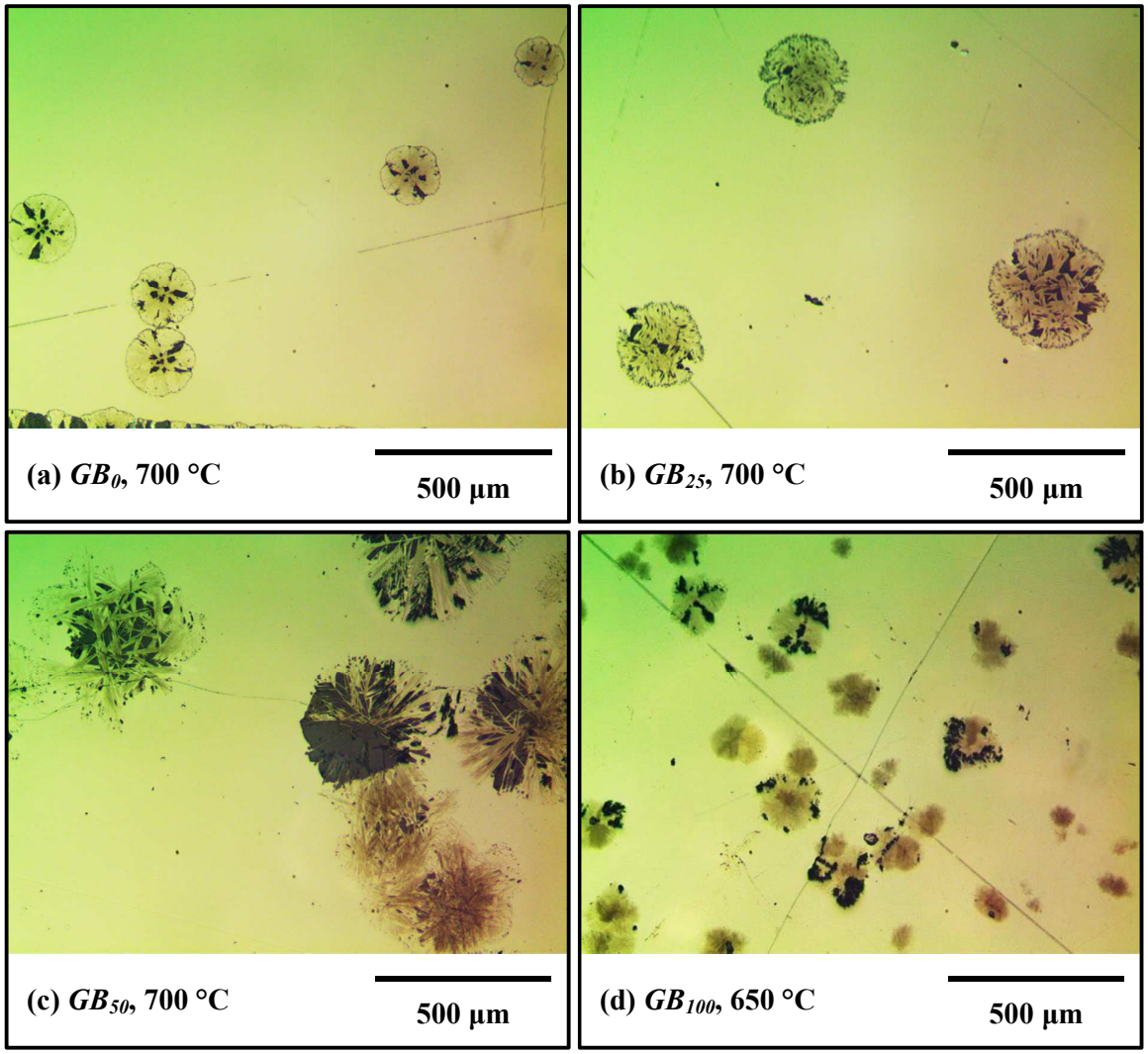
(a) GB_0, 700 °C
500 µm
(b) GB_{25}, 700 °C
500 µm
(c) GB_{50}, 700 °C
500 µm
(d) GB_{100}, 650 °C
500 µm

Fig. 9

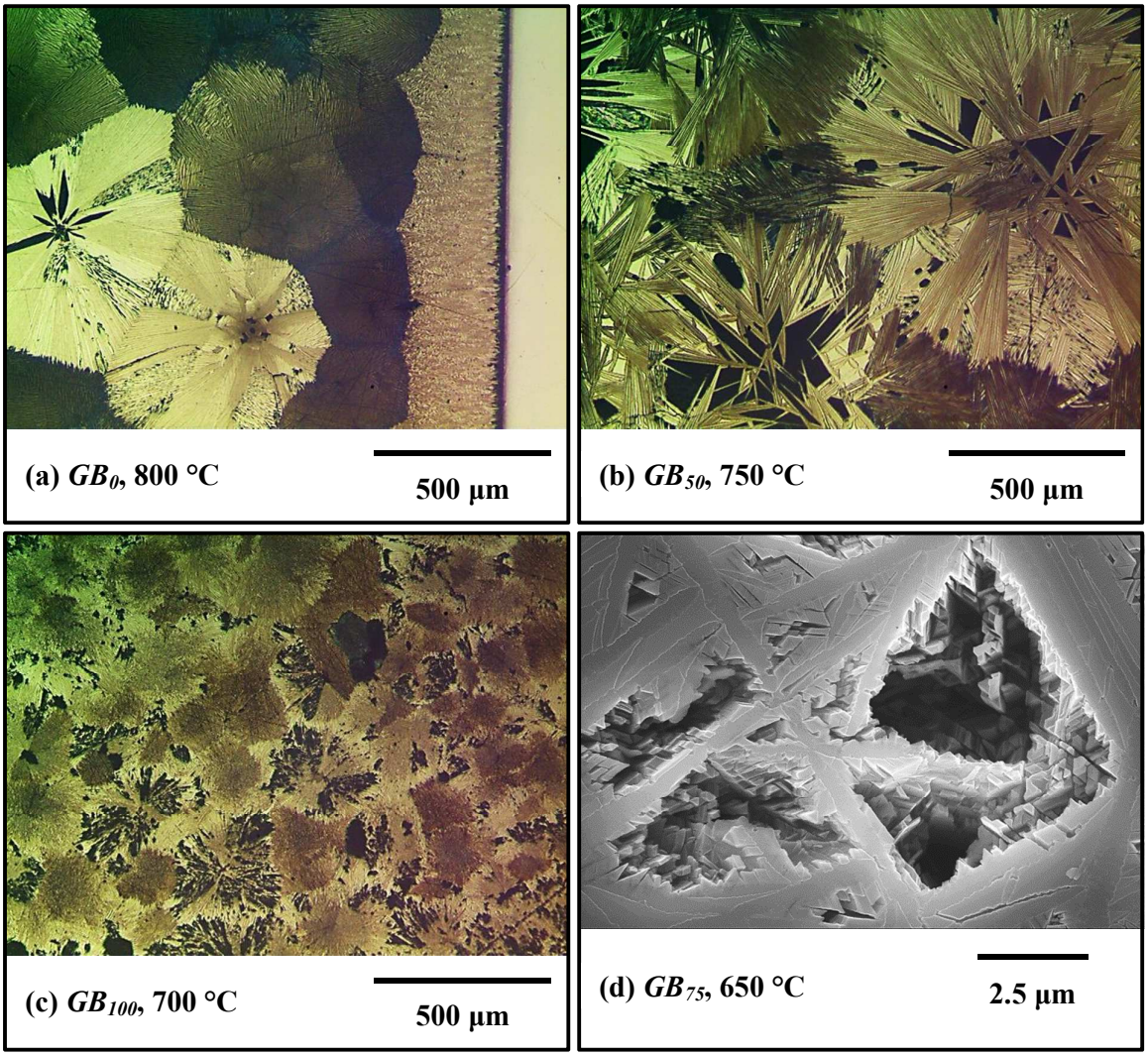
(a) GB_0, 800 °C
500 µm
(b) GB_{50}, 750 °C
500 µm
(c) GB_{100}, 700 °C
500 µm
(d) GB_{75}, 650 °C
2.5 µm

Fig. 10

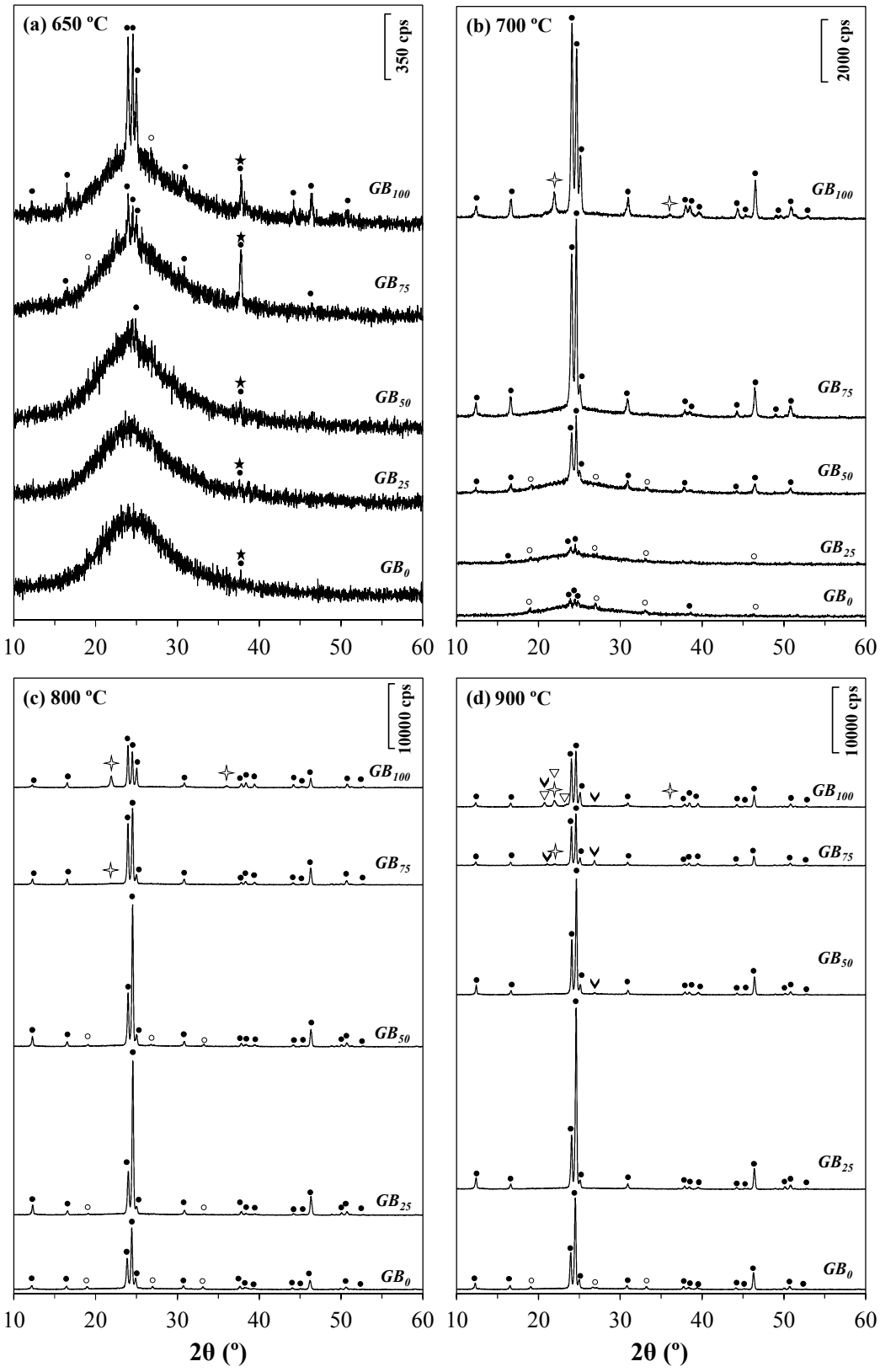
(a) 650 ºC
350 cps
GB100
GB75
GB50
GB25
GB0
(b) 700 ºC
2000 cps
GB100
GB75
GB50
GB25
GB0
(c) 800 ºC
10000 cps
GB100
GB75
GB50
GB25
GB0
(d) 900 ºC
10000 cps
GB100
GB75
GB50
GB25
GB0
10 20 30 40 50 60
2θ (º)

Fig. 11

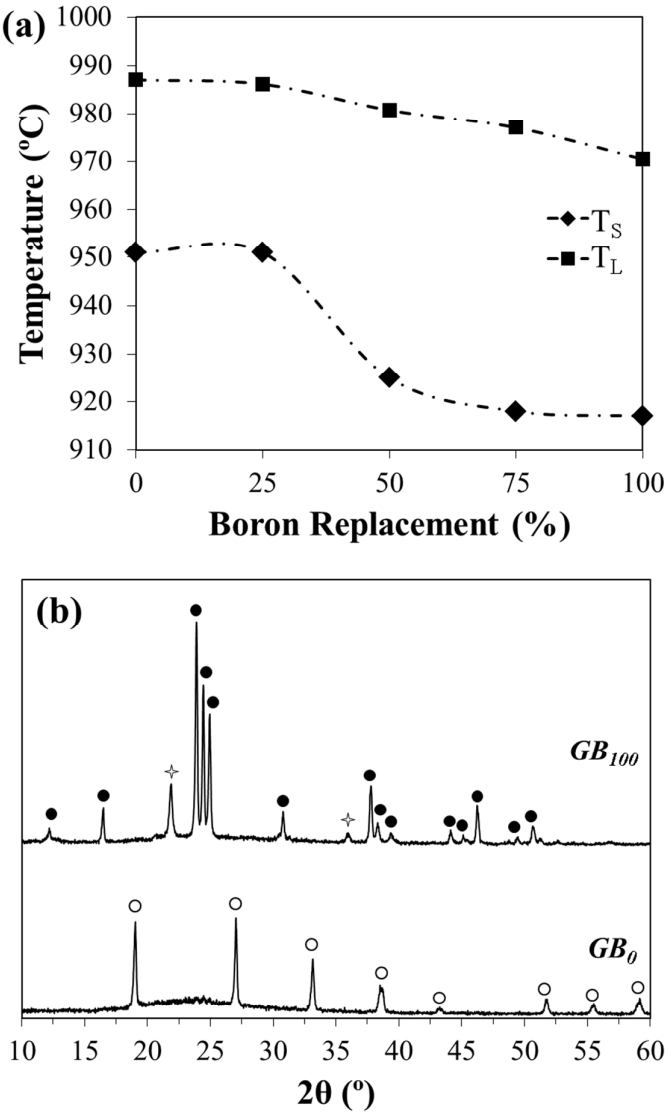

Fig. 12

Table 1 Compositions of the experimental glasses in mol%

	GB_0	GB_{25}	GB_{50}	GB_{75}	GB_{100}
Li_2O	23.00	23.00	23.00	23.00	23.00
K_2O	2.64	2.64	2.64	2.64	2.64
Al_2O_3	2.64	1.98	1.32	0.66	0.00
B_2O_3	0.00	0.66	1.32	1.98	2.64
SiO_2	71.72	71.72	71.72	71.72	71.72
$(B_2O_3) / (B_2O_3+Al_2O_3)$	0.00	0.25	0.50	0.75	1.00

Table 2 NMR parameters for ^{29}Si deconvolution.

	δ_{iso} *(ppm)*				*FWHM (ppm)*				**Amount** *(%)*			
	Q^2	Q^3	Q^4(*1*X)	Q^4	Q^2	Q^3	Q^4(*1*X)	Q^4	Q^2	Q^3†	Q^4(*1*X)	Q^4
GB_0	−78.5	−92.6	−103.4	−108.9	5.1	15.7	9.7	10.4	1	74	15	10
GB_{25}	″	″	″	″	8.5	″	10.7	10.3	3	70	16	11
GB_{50}	″	″	″	″	10.3	15.1	10.9	10.4	4	65	18	13
GB_{100}	″	″	−104.0	″	9.5	14.8	10.8	10.5	4	64	17	15

δ_{iso}: *Chemical shift*
FWHM: *Full width at half maximum*
X: *Al or B*
†: *Corresponds to both Q^3 and Q^4(3*Al)

Table 3 NMR parameters for ^{11}B deconvolution.

Boron Site	δ_{iso} (ppm)	Q_{CC} (MHz)	η	Amount (%)
***GB*$_{25}$**				
B^{IV}	–1.38	---	---	38.25
B^{IIIa}	17.00	2.64	0.42	46.45
B^{IIIs}	11.50	2.14	0.04	15.30
***GB*$_{50}$**				
B^{IV}	–1.36	---	---	43.28
B^{IIIa}	17.07	2.58	0.42	38.27
B^{IIIs}	11.48	2.34	0.04	18.45
***GB*$_{100}$**				
B^{IV}	–1.33	---	---	48.04
B^{IIIa}	17.41	2.63	0.35	38.81
B^{IIIs}	11.16	2.14	0.17	13.15

δ_{iso}: *Chemical shift*
Q_{CC}: *Quadrupolar coupling constant*
η: *asymmetry parameter*

Table 4 Properties of experimental glasses

	T_g	T_d	T_c	T_p	T_S	T_L	$T_c–T_g$	T_{gr}	K_H	Density	Oxygen Density	Molar volume	CTE	Band Gap Energy	NBO
	(°C)									(g cm^{-3})		(cm^3 mol^{-1})	×10^{-6} K^{-1}	eV	%
GB$_0$	480	522	707	824	951	987	227	0.598	0.93	2.35 ± 0.003	1.209 ± 0.002	23.43 ± 0.03	9.6	3.80	26.0
GB$_{25}$	480	507	703	812	952	986	223	0.598	0.89	2.36 ± 0.003	1.216 ± 0.001	23.29 ± 0.03	9.9	3.83	26.4
GB$_{50}$	480	514	699	797	925	981	219	0.601	0.97	2.36 ± 0.002	1.220 ± 0.001	23.21 ± 0.02	10.1	3.86	26.8
GB$_{75}$	479	501	688	767	918	977	209	0.602	0.91	2.36 ± 0.002	1.226 ± 0.001	23.09 ± 0.02	9.9	3.86	---
GB$_{100}$	476	497	679	768	917	970	203	0.602	0.85	2.36 ± 0.003	1.233 ± 0.002	22.97 ± 0.03	10.0	3.89	27.5